Supporting Information for

Synergistic Mediation of Dual Donor Levels in CNS/BOCB-OV Heterojunctions for Enhanced Photocatalytic CO_2 Reduction

Ruiming Fang[a,b,c], Zhongqing Yang[a,b*], Jiajun Sun[c], Chenxuan Zhu[a,b], Yanglin Chen[c], Ziqi Wang[a,b], Can Xue[c*]

[a] Key Laboratory of Low-grade Energy Utilization Technologies and Systems, Ministry of Education of PRC, Chongqing University, Chongqing, 400044, China

[b] School of Energy and Power Engineering, Chongqing University, Chongqing, 400044, China

[c] School of Materials Science and Engineering, Nanyang Technological University, 50 Nanyang Avenue, 639798, Singapore

* Corresponding author:

Zhongqing Yang

E-mail: zqyang@cqu.edu.cn

* Corresponding author:

Can Xue

E-mail: cxue@ntu.edu.sg

Table of Contents

1. Materials and chemicals

$Bi(NO_3)_3\cdot 5H_2O$ (AR, ≥ 99.0%), KCl (AR, ≥ 99.5%), KBr (AR, ≥ 99.0%), Ethylene glycol (GC, ≥ 99.0%), Melamine (AR, ≥ 99.0%), Polyethylene Glycol (PEG, AR, ≥ 99.0%) and Deionized water were obtained from Aladdin Chemical Reagent Co., Ltd. High-purity CO_2 (99.999%), High-purity Ar (99.999%) were obtained from Chongqing Ruike Gas Co., Ltd.

2. Catalytic Characterization

In this study, SEM, TEM, XRD, FTIR, XPS, UV-Vis, PL, I-t and In-situ FTIR were used to analyze the catalyst morphology, the structure of surface topography, the properties of elements and the photoelectric characteristics.

X-ray diffraction (XRD) patterns were obtained on the X-ray powder diffractometer (BRUCKER D8 ADVANCE) with the 10~90° scan range at the rate of 8°/min. The Chemical structure and functional groups of the photocatalysts were collected on FTIR Spectrometer (Nicolet IS10), the scanning range and resolution were 400~4000 cm^{-1} and 4 cm^{-1}, respectively. Scanning electron microscopy (SEM) images were shotted by GeminiSEM 300 field emission scanning electron microscope. Transmission Electron Microscopy (TEM) images were shotted by FEI Talos F200X (FEI Corporation, American) field emission transmission electron microscope. X-ray photoelectron spectroscopy (XPS) data were recorded on a Thermo escalab 250Xi photoelectron spectrometer, and the binding energy was corrected according to C 1s peak at 284.8 eV as internal standard. Photoluminescence spectra (PL) characterization was conducted on an FLS1000/FSS steady state transient fluorescence spectrometer at room temperature. UV-vis absorption spectra were obtained using a UV-3600 ultraviolet-visible near-infrared spectrophotometer. Transient photocurrent characterization was conducted on an electrochemical workstation (CHI-760E, Chenhua, Shanghai China).

In-situ DRIFTS analyses is performed in an infrared spectrometer (Vertex 70v, Bruker, Germany) equipped with an MCT detector. The sample is painted on the substrate and vacuum treated for 30 min to remove impurity gas. CO_2 and trace water vapor are introduced into the reaction chamber. After standing in the dark for 30 min, the sample is irradiated under a light source for 60 min, and infrared spectrum data is collected at regular intervals.

3. Reaction Condition and Activity Evaluation

The gas-solid heterogeneous visible light reduction reaction was carried out in a sealed photocatalytic reaction system equipped with a vacuum system and a constant temperature water cooling system. In a typical experiment, the catalyst (0.015 g) was dispersed uniformly on a quartz slide with the area of 12 cm^2. The quartz slide was placed on the glass support in the photocatalytic reactor. After placing the catalyst, 10 mL deionized water was injected into the sealed container and then purged with high purity CO_2 for 30 min. Vacuum first, then filled with high purity CO_2, repeated three times to remove impurities in the reactor and water. After the last inflation, adjusted the pressure to normal pressure and closed the valves. Before the reaction, 1 mL gas was collected from the sampling port and detected by gas chromatography to ensure no impurities left in the reactor. Then, after turning on the constant temperature water cooling system and standing for 10 min, turned on the light source switch and started the photocatalytic reaction. The samples were collected manually every hour and analyzed by gas chromatography (Techcomp 7900). During the photocatalytic process, the whole system was maintained at 25℃.

The temperature changes in the heterojunction and its individual components over time under visible light irradiation represent the variations during the reaction process. The specific measurement process involves initial calibration of the infrared camera, followed by the uniform dispersion of the catalyst on a 12cm^2 quartz carrier according to the standard photocatalytic reaction procedure. Subsequently, the thermal imager is activated, focused on the surface where the photocatalytic reaction occurs. Simultaneously, the experimental system's circulating water cooling system is activated to stabilize the surface temperature of the catalyst in the dark environment, which is then recorded. Upon turning on the light source, the infrared image of the sample surface is captured throughout the reaction process, allowing the recording of changes in surface temperature distribution over time.

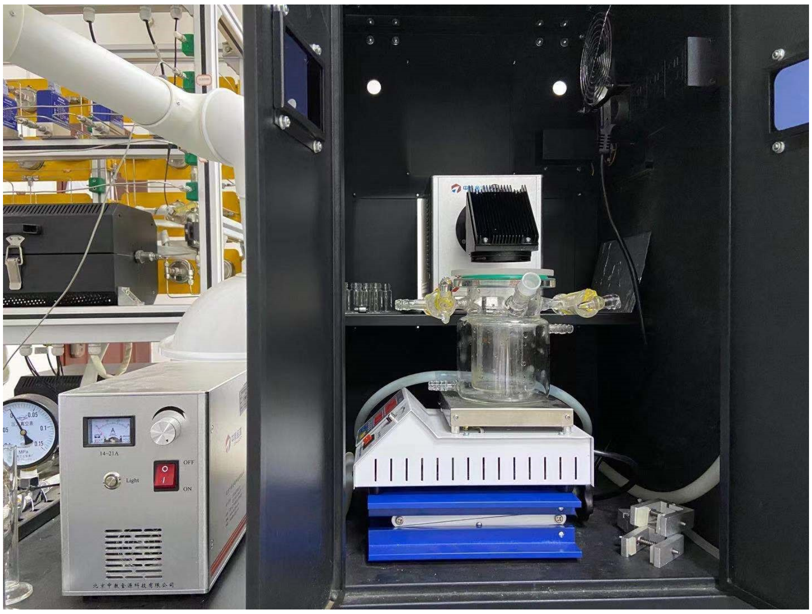

Fig. S1. The device picture of photocatalytic reduction of CO_2 reaction.

4. Density Functional Theory (DFT) Calculations

Density functional theory (DFT) calculations were performed using the CASTEP module of Material Studio 8.0. The generalized gradient approximation PBE functional in GGA for the exchange correlation between electrons, combined with the super-soft pseudopotential (USP) for the relationship between valence electrons and ion. The convergence standard values of self-consistent iteration energy, atomic force, stress and atomic displacement were set to 1.0×10^{-5} eV/atom, 0.03 eV $Å^{-1}$, 0.05 GPA and 0. 001 Å, respectively. The plane wave cutoff energy is set to 500 eV, and the K grid is set to 3 × 3 × 1. Additionally, in the DFT calculation, CNS, CNSNV, BOCB, BOCB-OV, CNS/BOCB, and CNSNV/BOCB-OV respectively correspond to CNS, CNS-HT, BOCB, BOCB-OV, CNS/BOCB, and CNS/BOCB-OV in the prepared sample.

5. Formula

$\tau=(A_1\tau_1^2+A_2\tau_2^2)/ A_1\tau_1+A_2\tau_2$ Formula S1

where A_1 and A_2 are the corresponding amplitudes, and τ_1 and τ_2 are the fluorescent lifetimes.

$\alpha hv=a(hv-Eg)^{n/2}$ Formula S2

where α is the absorption constant of the semiconductor, h is the Planck constant, v is the photon frequency, and Eg is the bandgap. Since all four samples are indirect bandgap semiconductors, n is taken as 4.

$E_{VB,NHE}=\phi+E_{VB,XPS}-4.44$ Formula S3

where ϕ represents the instrument work function (4.2 eV), and $E_{VB,XPS}$ represents the XPS valence band spectrum tangent value.

$E_{CB}=E_{VB}-E_g$ Formula S4

where E_{CB} represents the conduction band potential, E_{VB} represents the valence band potential, and E_g represents the band gap, determined from the optical absorption

$\Phi = E_{vac} - E_f$ Formula S5

where E_{vac} and E_f represent the vacuum energy level and the Fermi level, respectively

6. Supplementary Figures

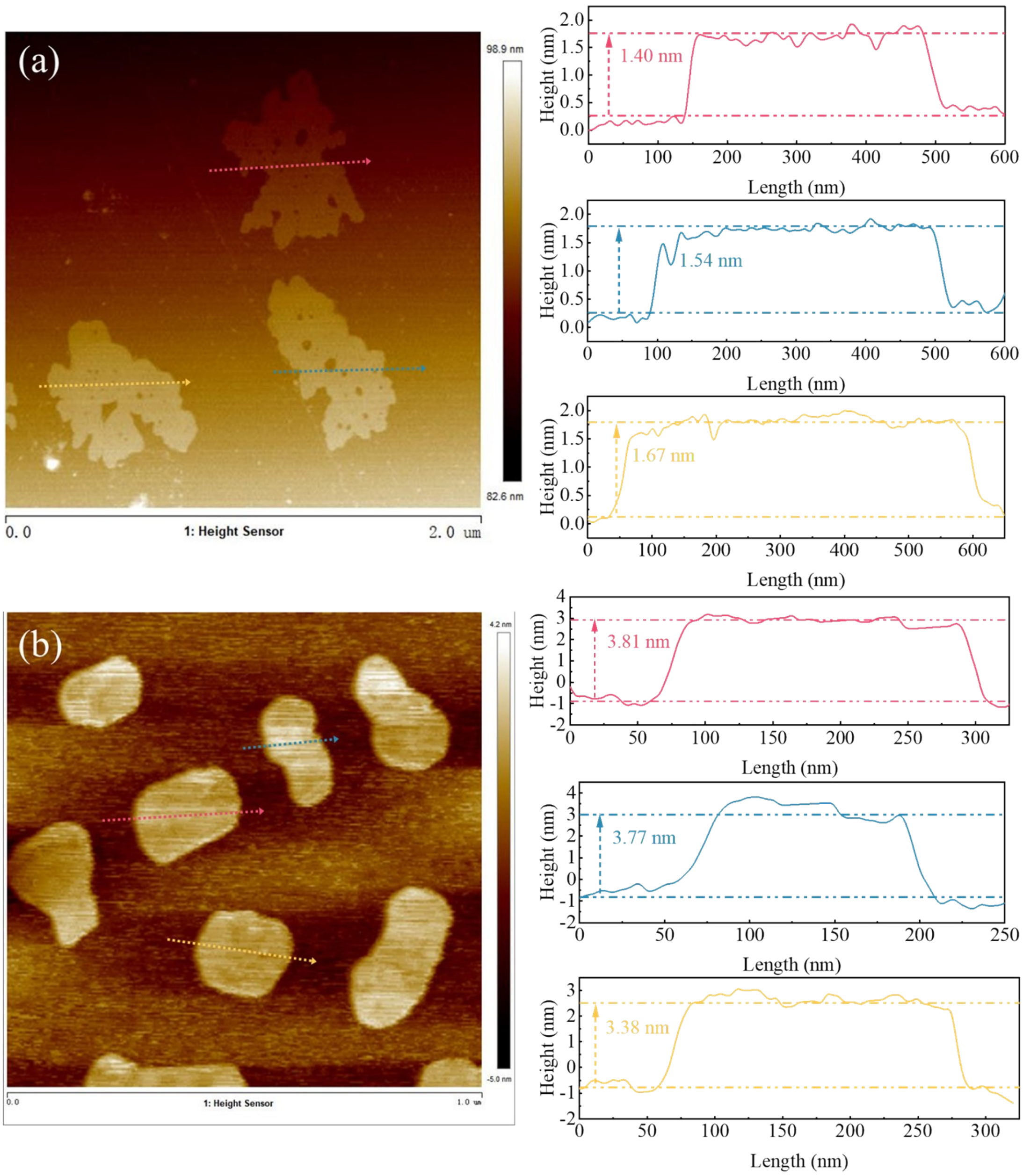

Fig. S2. Atomic Force Microscope pattern and corresponding thickness analysis of (a) CNS and (b) BOCB-OV

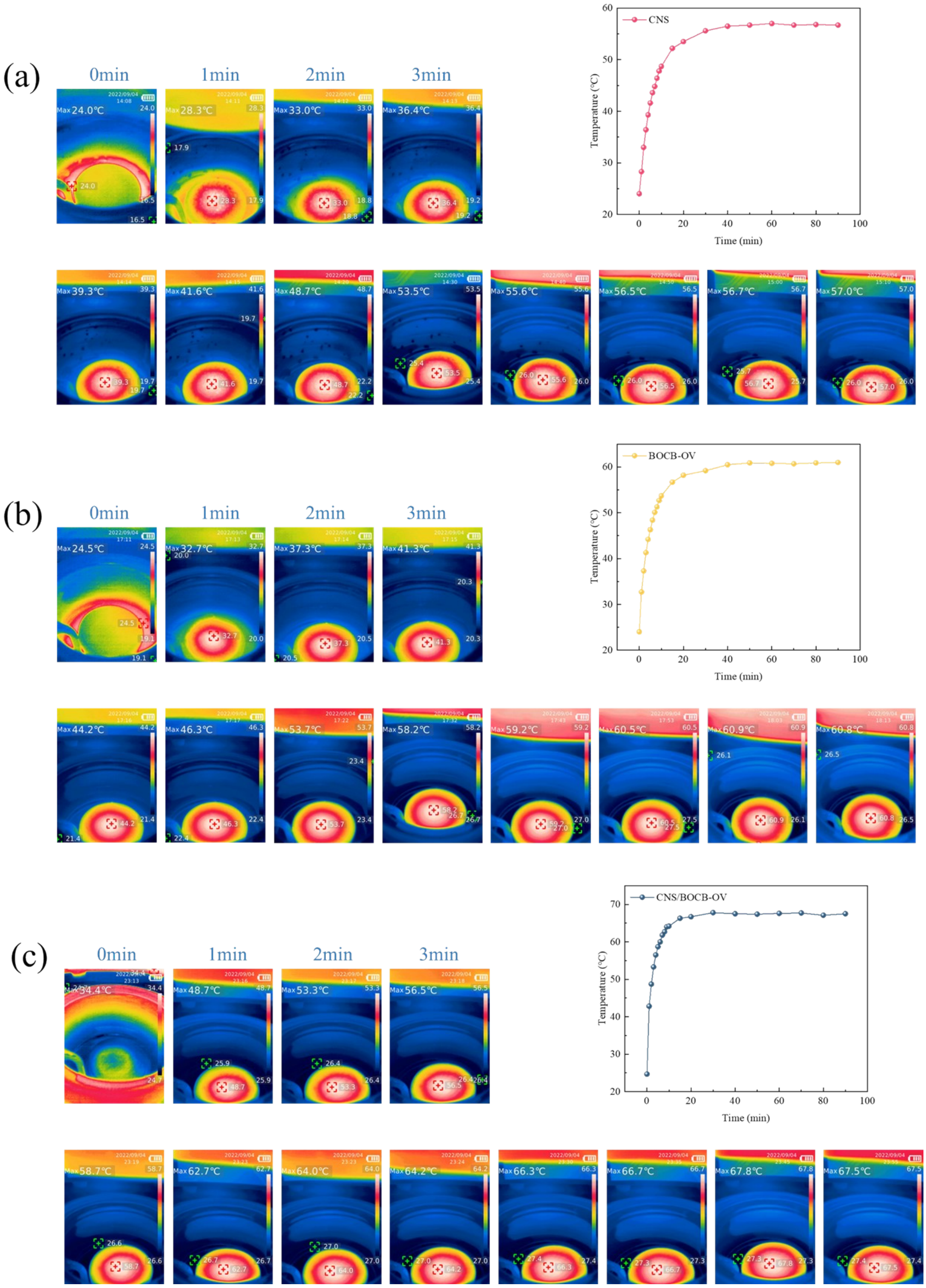

Fig. S3. (a) CNS; (b) BOCB-OV; (c) CNS/BOCB-OV Variation of surface temperature with time under Visible Light

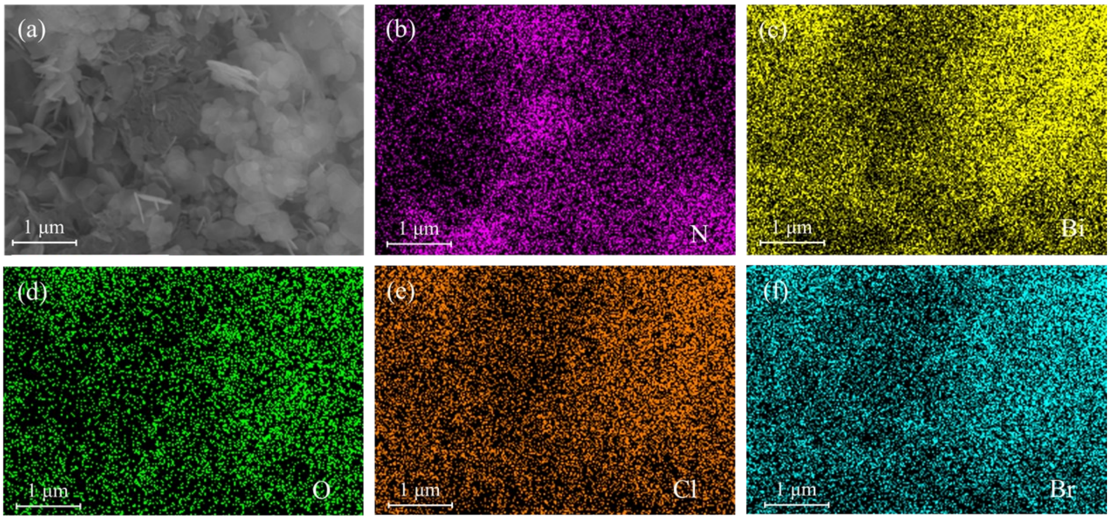

Fig. S4. (a)-(f) the N, Bi, O, Cl, Br elemental mapping

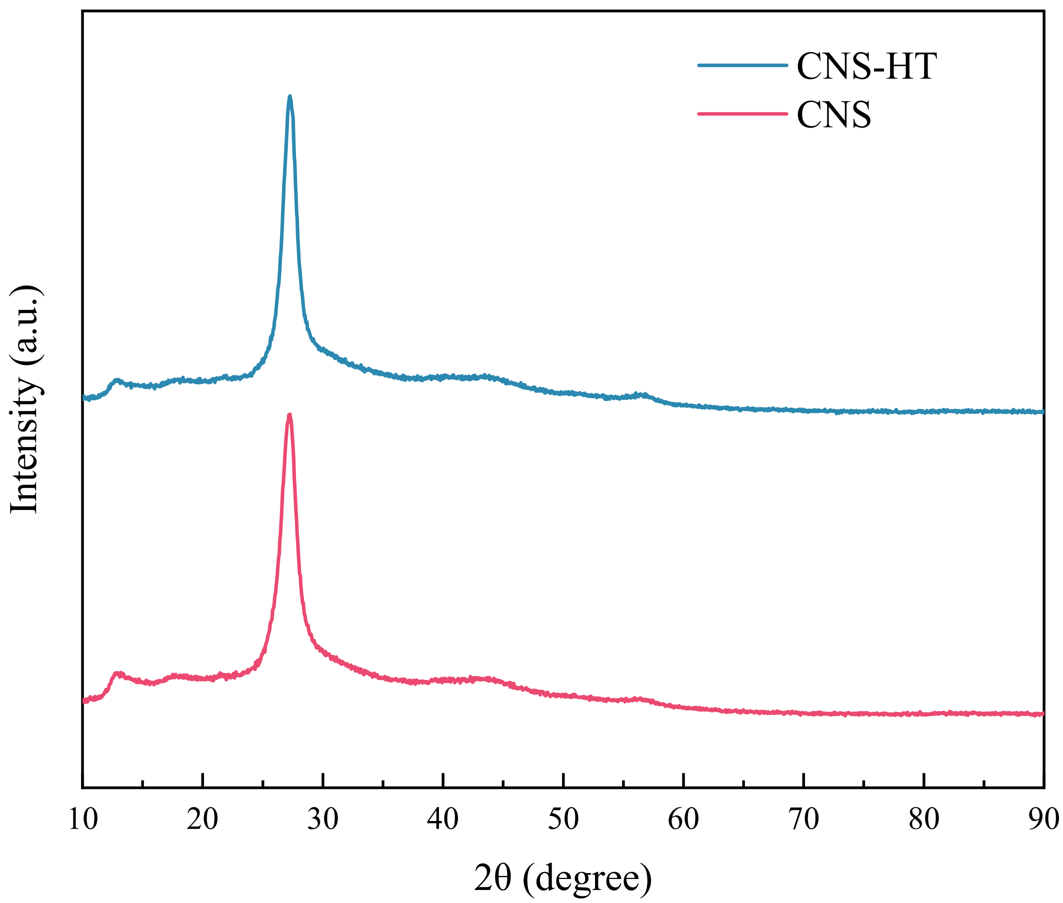

Fig. S5. XRD patterns of CNS and CNS-HT

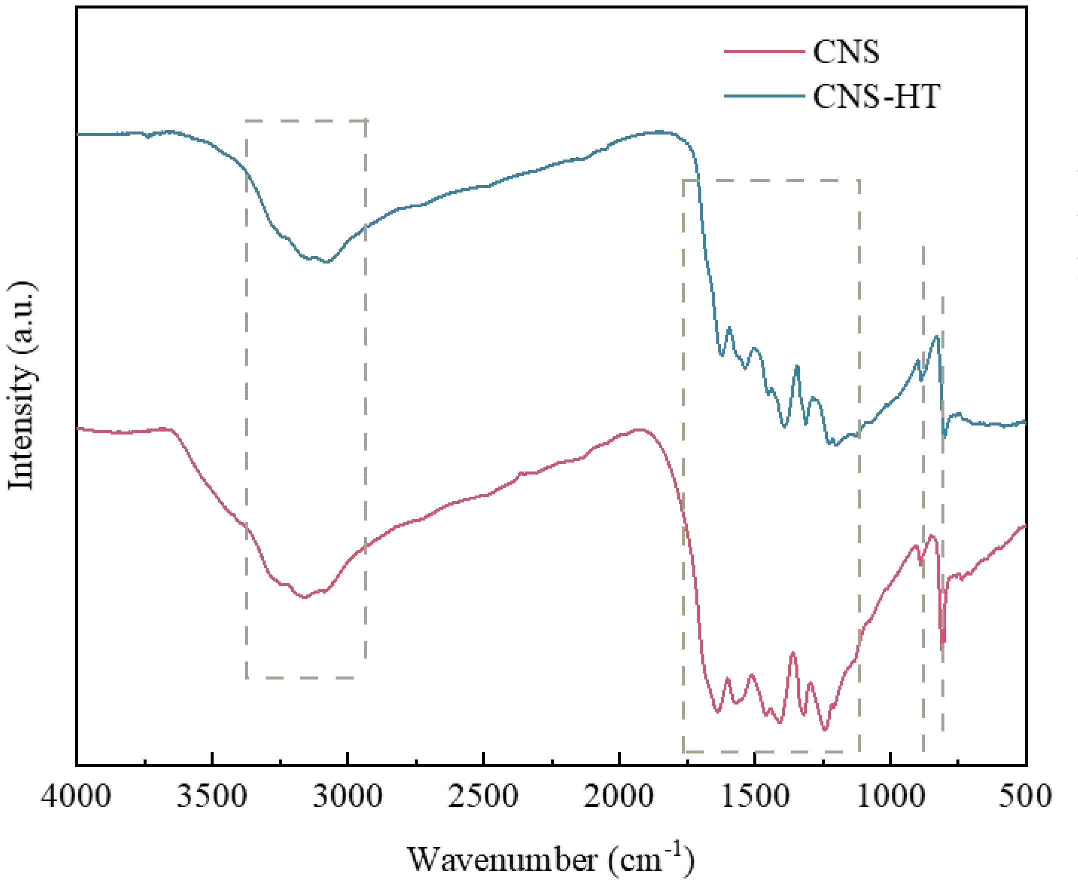

Fig. S6. FTIR patterns of CNS and CNS-HT

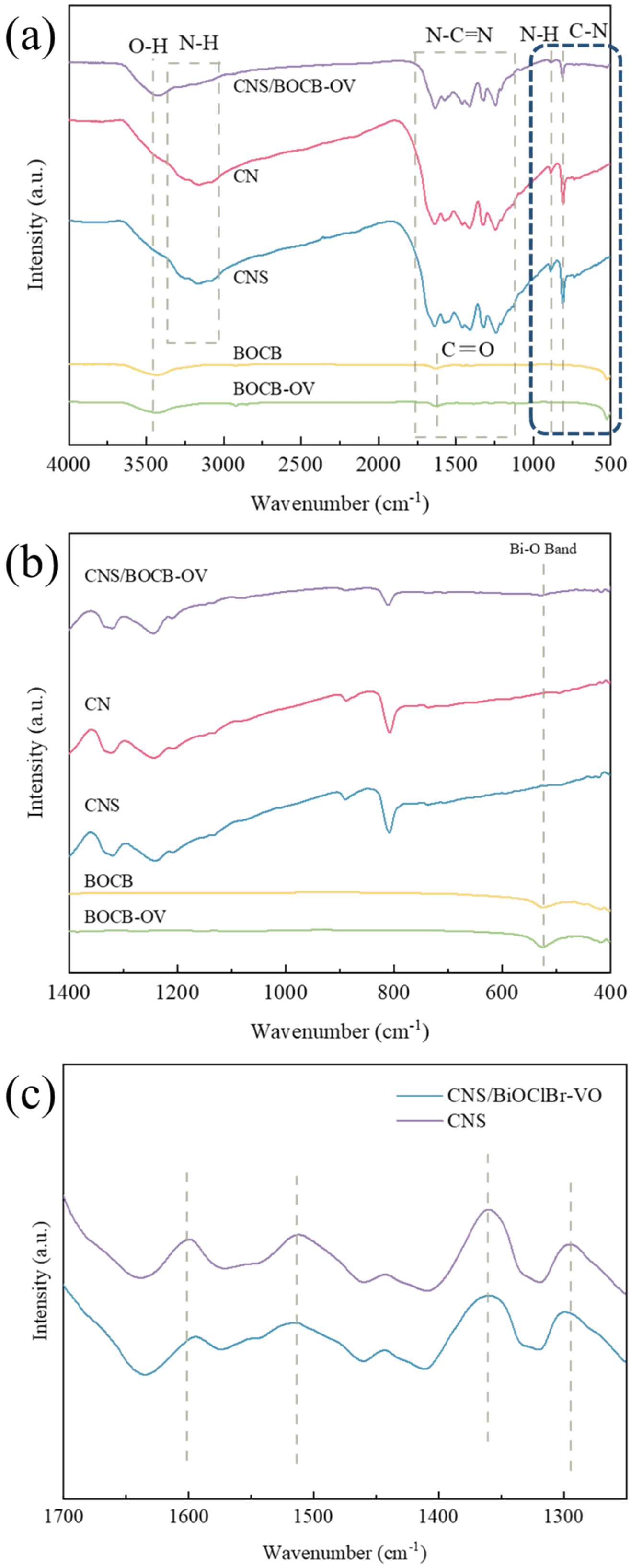

Fig. S7. FTIR patterns of CN, CNS, BOCB, BOCB-OV and CNS/BOCB-OV

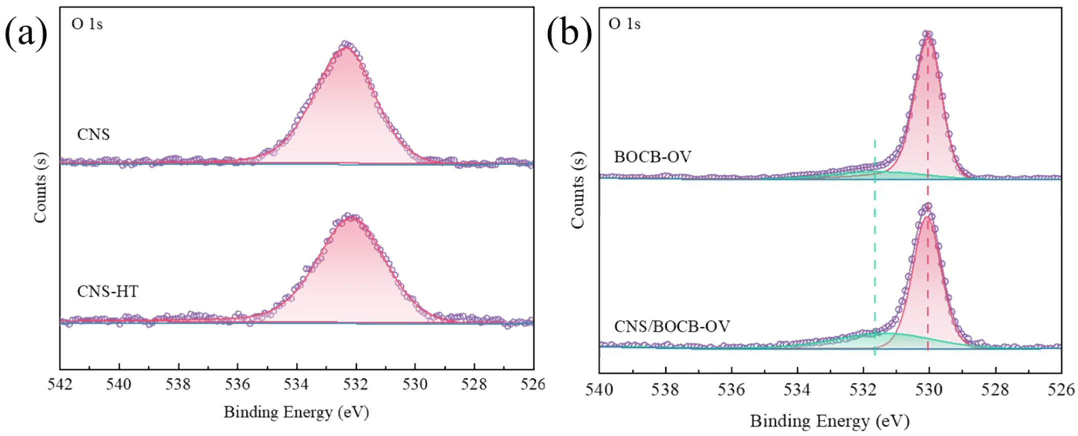

Fig. S8. High resolution XPS spectra of O 1s regions of (a) CNS and CNS-HT; (b) BOCB-OV, CNS/BOCB-OV

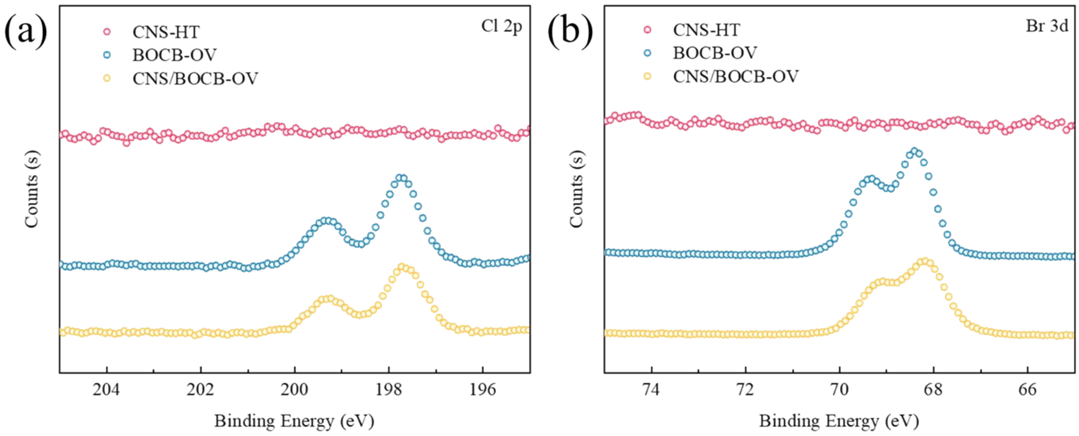

Fig. S9. High resolution XPS spectra of (a) Cl 2p regions and (b) Br 3d regions of CNS-HT, BOCB-OV, CNS/BOCB-OV

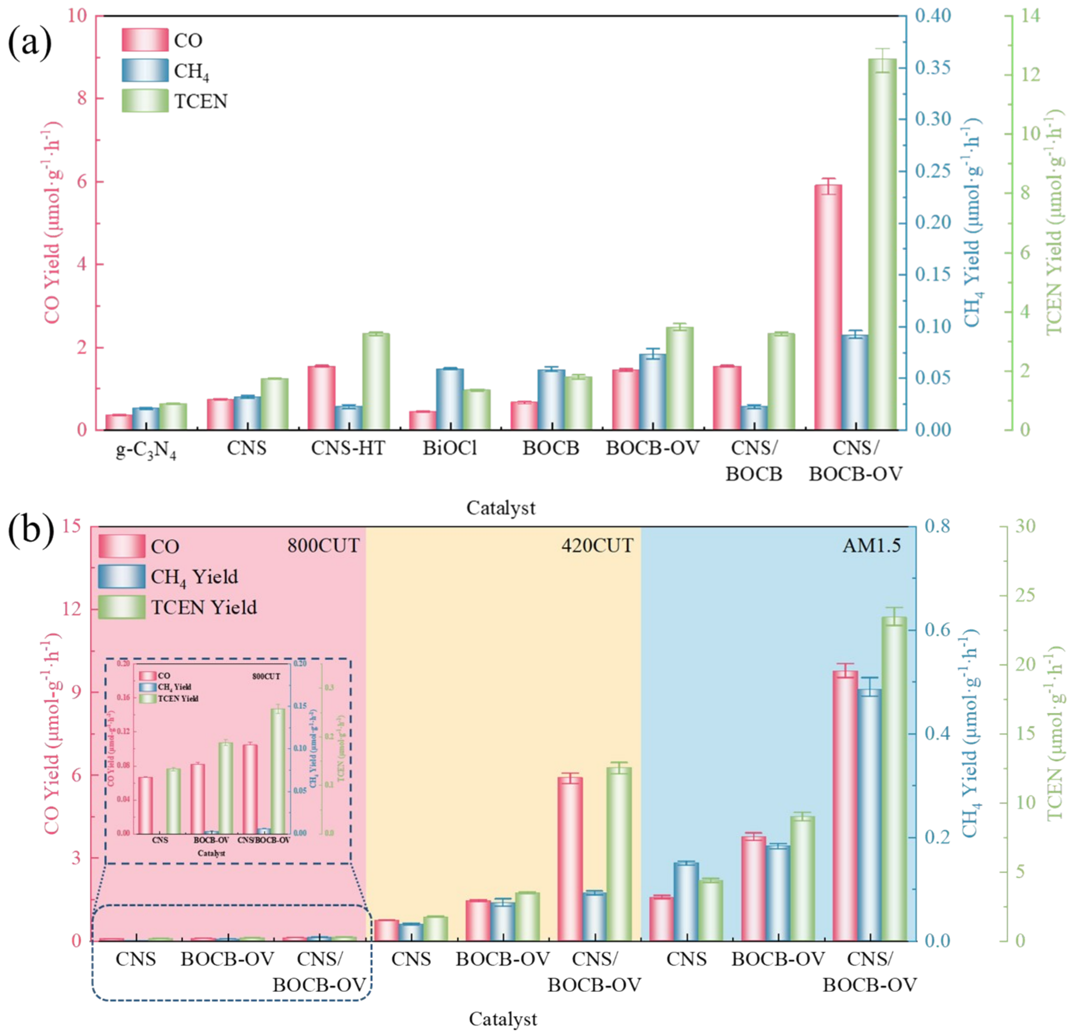

Fig. S10. Performance analysis of (a) g-C_3N_4, CNS, BiOCl, BiOBr, BOCB, BOCB-OV, CNS/BOCB and CNS/BOCB-OV under visible light irradiation; Performance analysis of (b) CNS, BOCB-OV and CNS/BOCB-OV under infrared light, visible light, simulated sunlight irradiation

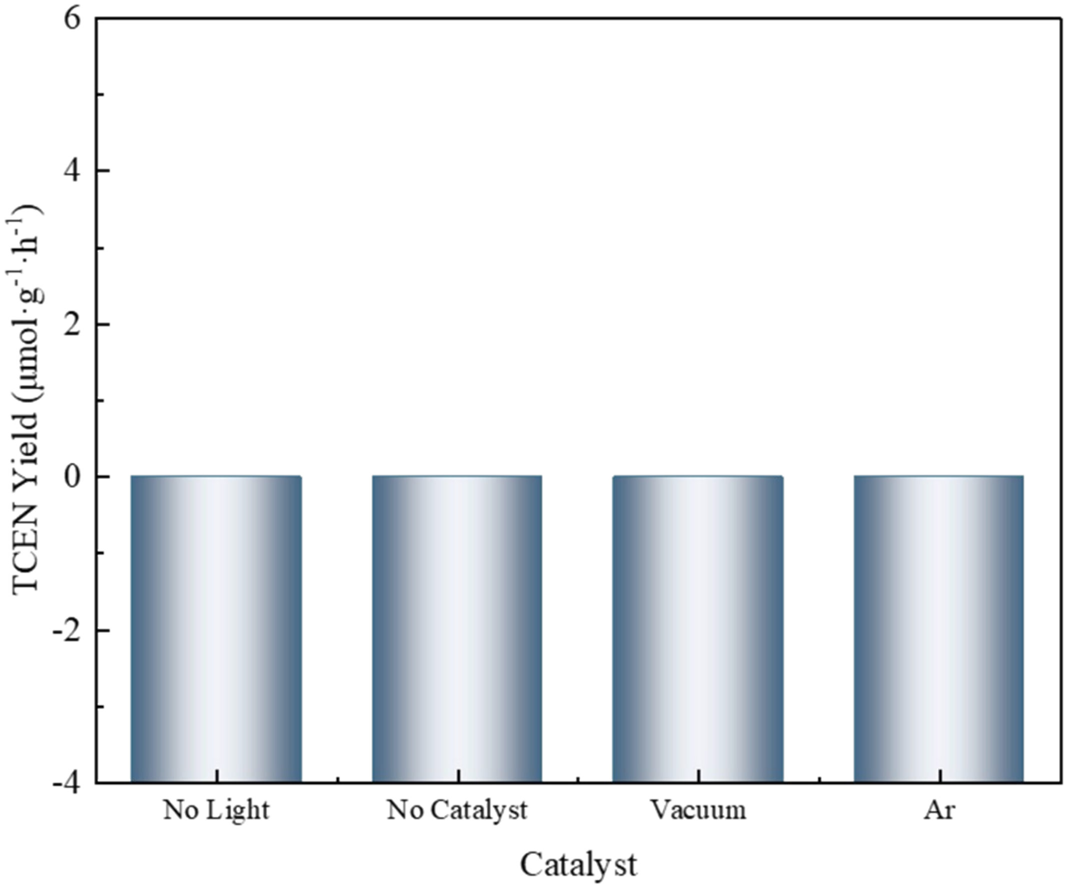

Fig. S11. Performance of CNS/BOCB-OV under different reaction conditions

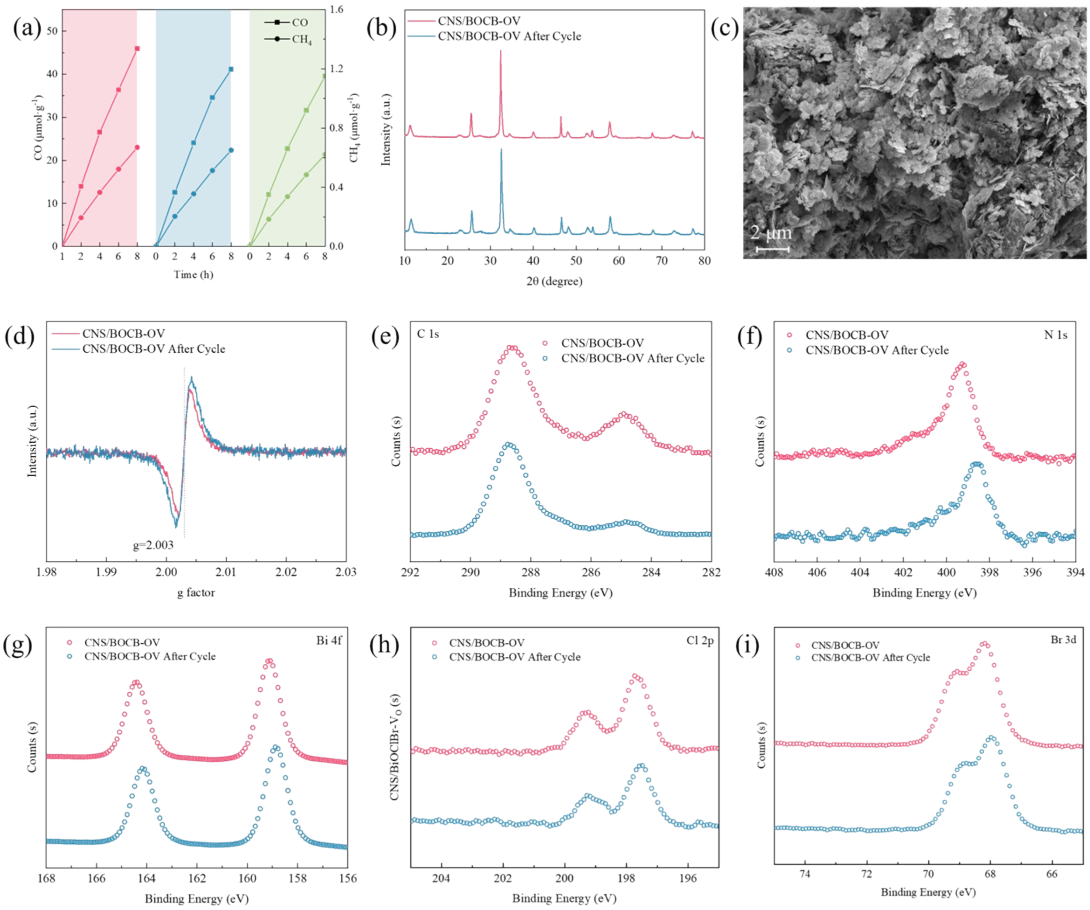

Fig. S12. (a) The reusability experiment of CNS/BOCB-OV under the light irradiation; (b) the SEM picture and (c) the XRD pattern of CNS/BOCB-OV after cycle; (d) EPR spectra of CNS/BOCB-OV and CNS/BOCB-OV after cycle experiments; High resolution XPS spectra of (e) C 1s regions; (f) N 1s regions; (g) Bi 4f regions; (h) Cl 2p regions and (i) Br 3d regions of CNS/BOCB-OV and CNS/BOCB-OV after cycle experiments

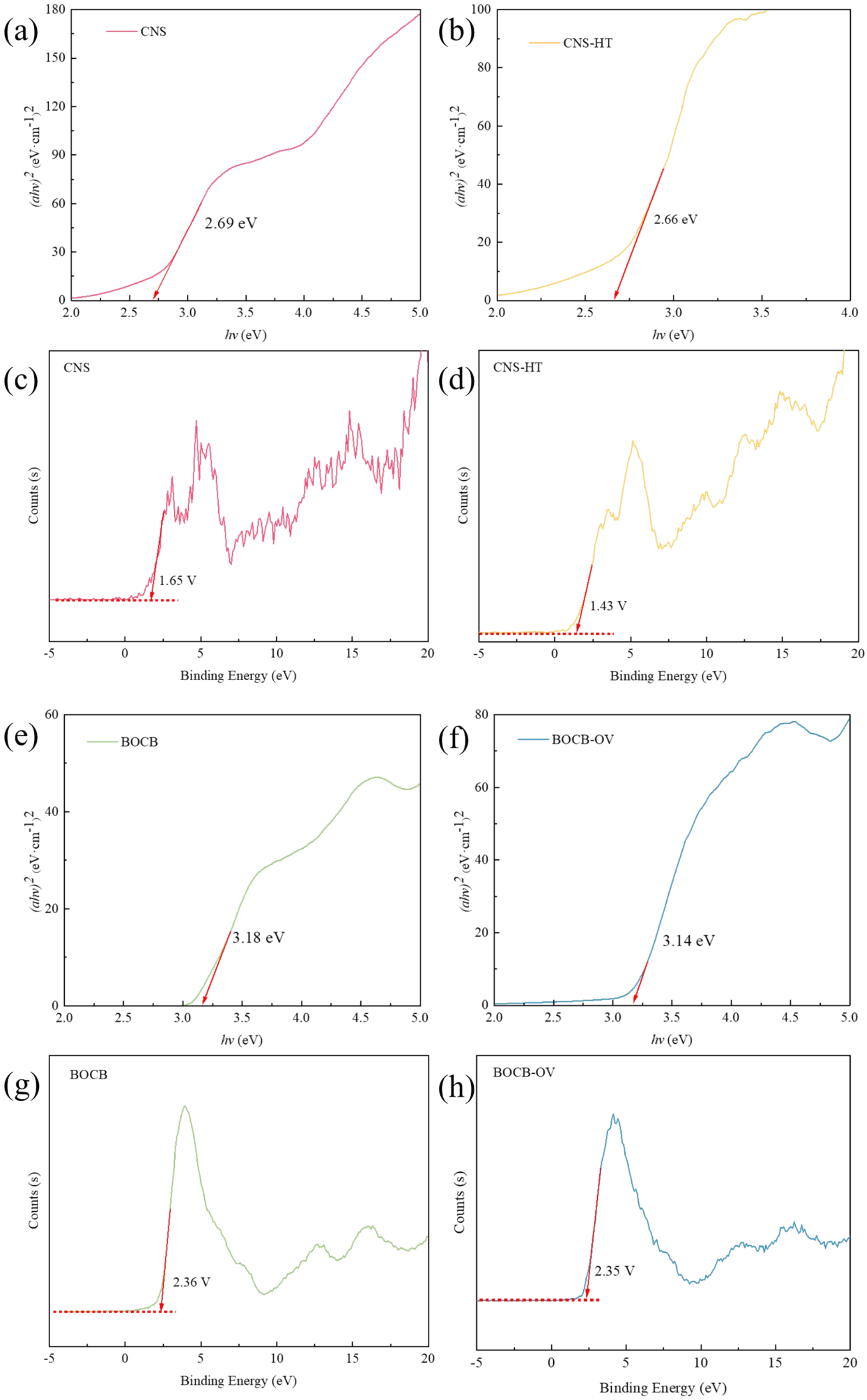
(a)
CNS
2.69 eV
$(\alpha h\nu)^2$ (eV·cm^{-1})^2
$h\nu$ (eV)
(b)
CNS-HT
2.66 eV
(c)
CNS
1.65 V
Counts (s)
Binding Energy (eV)
(d)
CNS-HT
1.43 V
(e)
BOCB
3.18 eV
(f)
BOCB-OV
3.14 eV
(g)
BOCB
2.36 V
(h)
BOCB-OV
2.35 V

Fig. S13. Bandgap calculation of (a) CNS; (b) CNS-HT; (e) BOCB and (f) BOCB-OV through "Tauc plot" method; XPS valence band spectrum of (c) CNS; (d) CNS-HT; (g) BOCB and (h) BOCB-OV

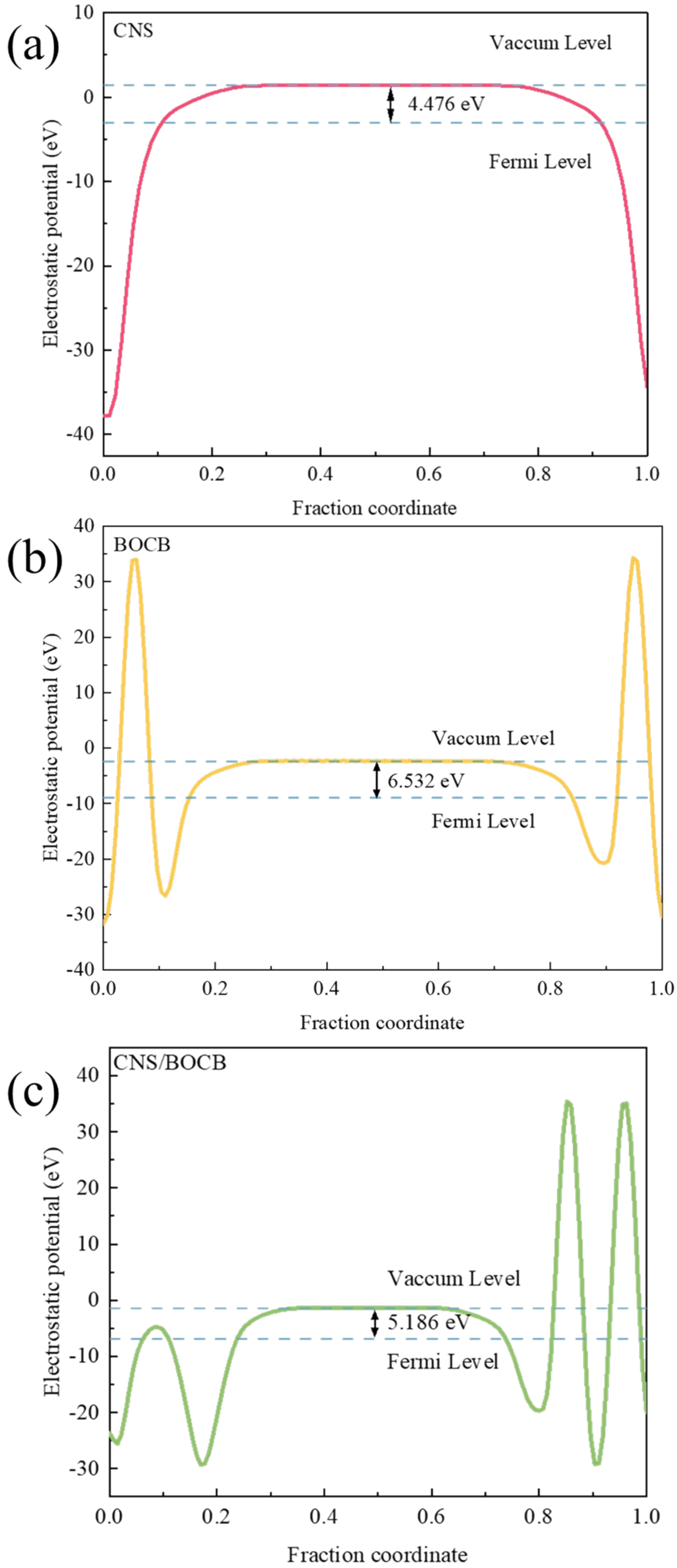

Fig. S14. Work functions of (a) CNS; (b) BOCB; and (c) CNS/BOCB hetero-junction

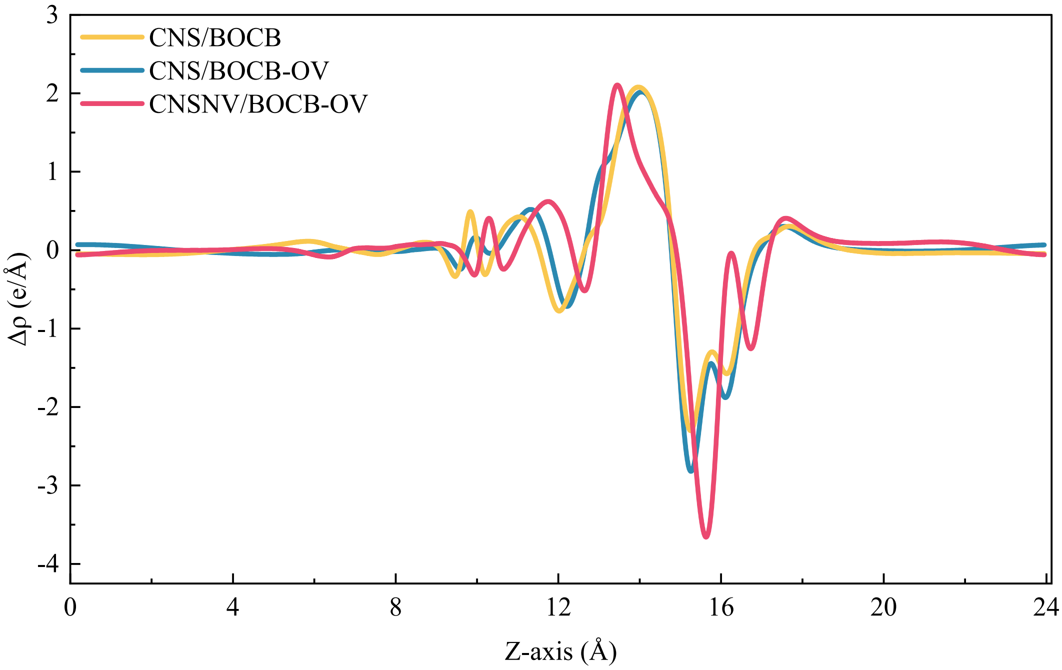

Fig. S15. Axial integral comparison plot of electron differential density of the three samples

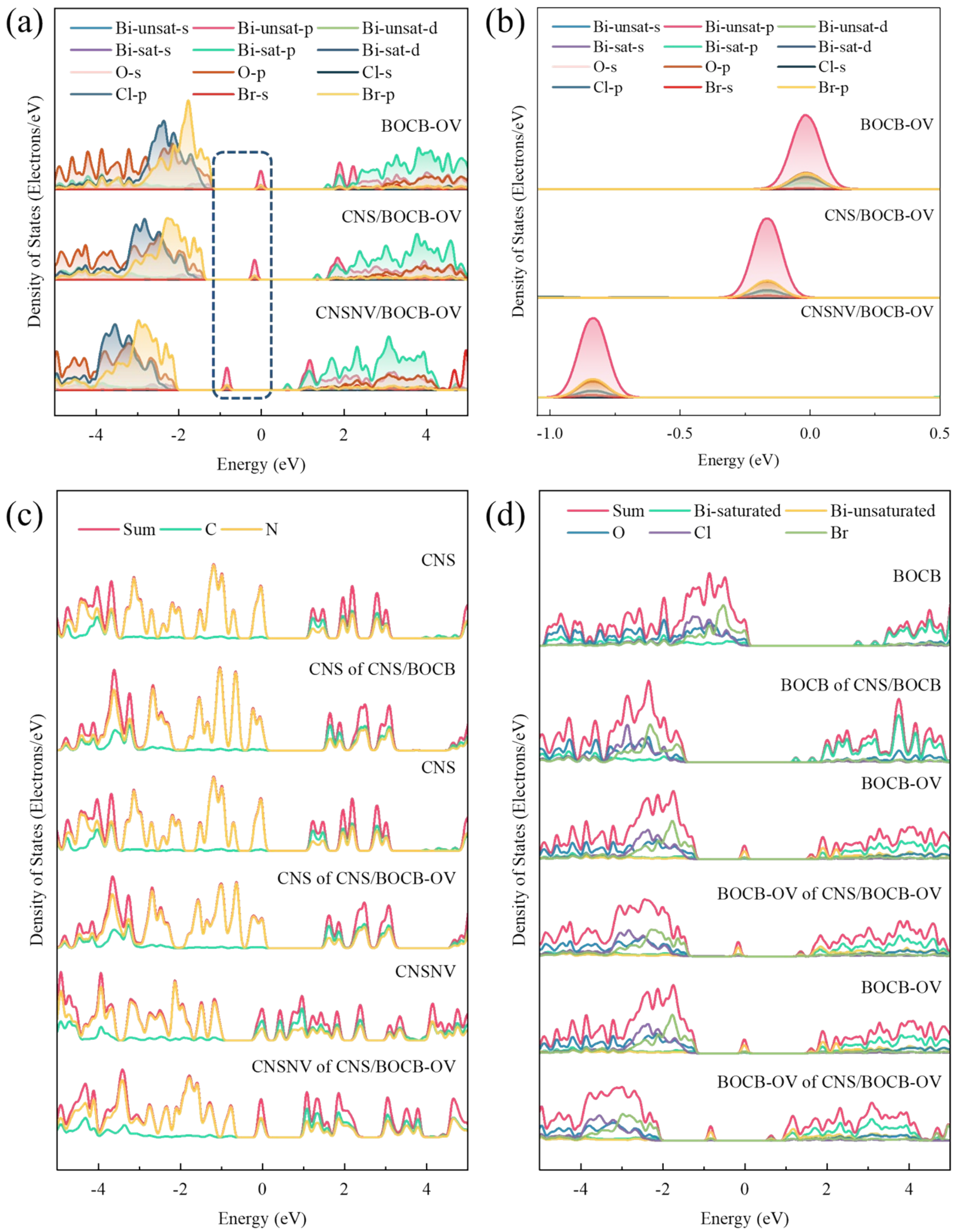

Fig. S16. (a) comparison of partial density of states of BOCB-OV before and after CNS/BOCB-OV and CNSNV/BOCB-OV heterojunction formation; (b) partial enlarged view of the intermediate energy level of BOCB, CNS/BOCB-OV and CNSNV/BOCB-OV; (c) comparison of density of states of CNS, CNSNV before and after CNS/BOCB-OV and CNSNV/BOCB-OV heterojunction formation; (d) comparison of density of states of BOCB, BOCB-OV before and after CNS/BOCB-OV and CNSNV/BOCB-OV heterojunction formation

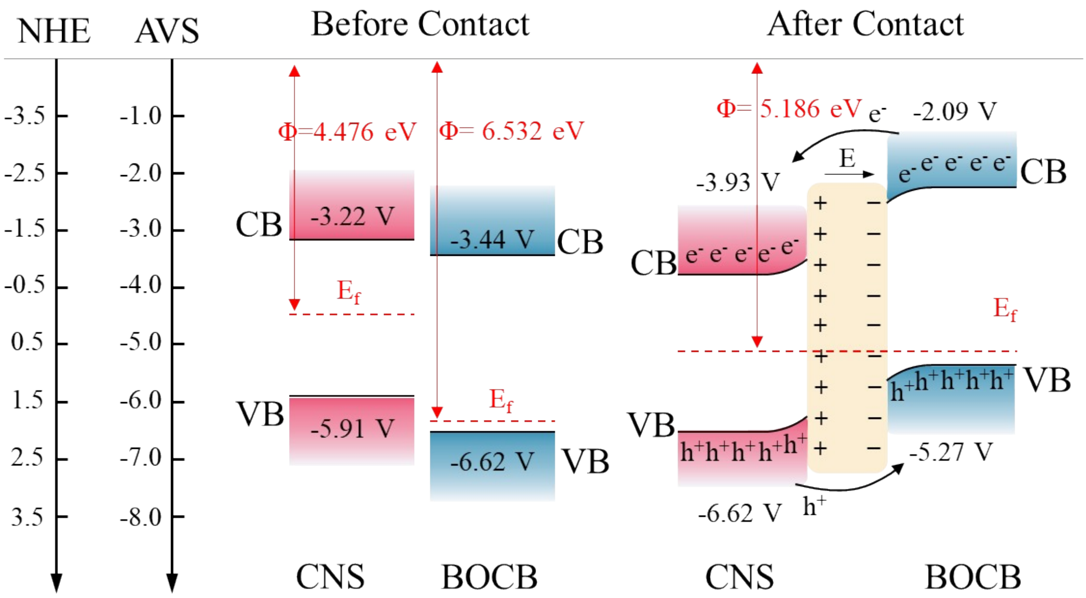

Fig. S17. Band edge of individual CNS, BOCB and CNS/BOCB heterojunction after interfaces contact (converted to the Absolute Vacuum Scale for clear comparison, Φ represents the work function, Ef represents the Fermi level, CB represents the conduction band, VB represents the valence band, and the arrow represents the electron flow direction)

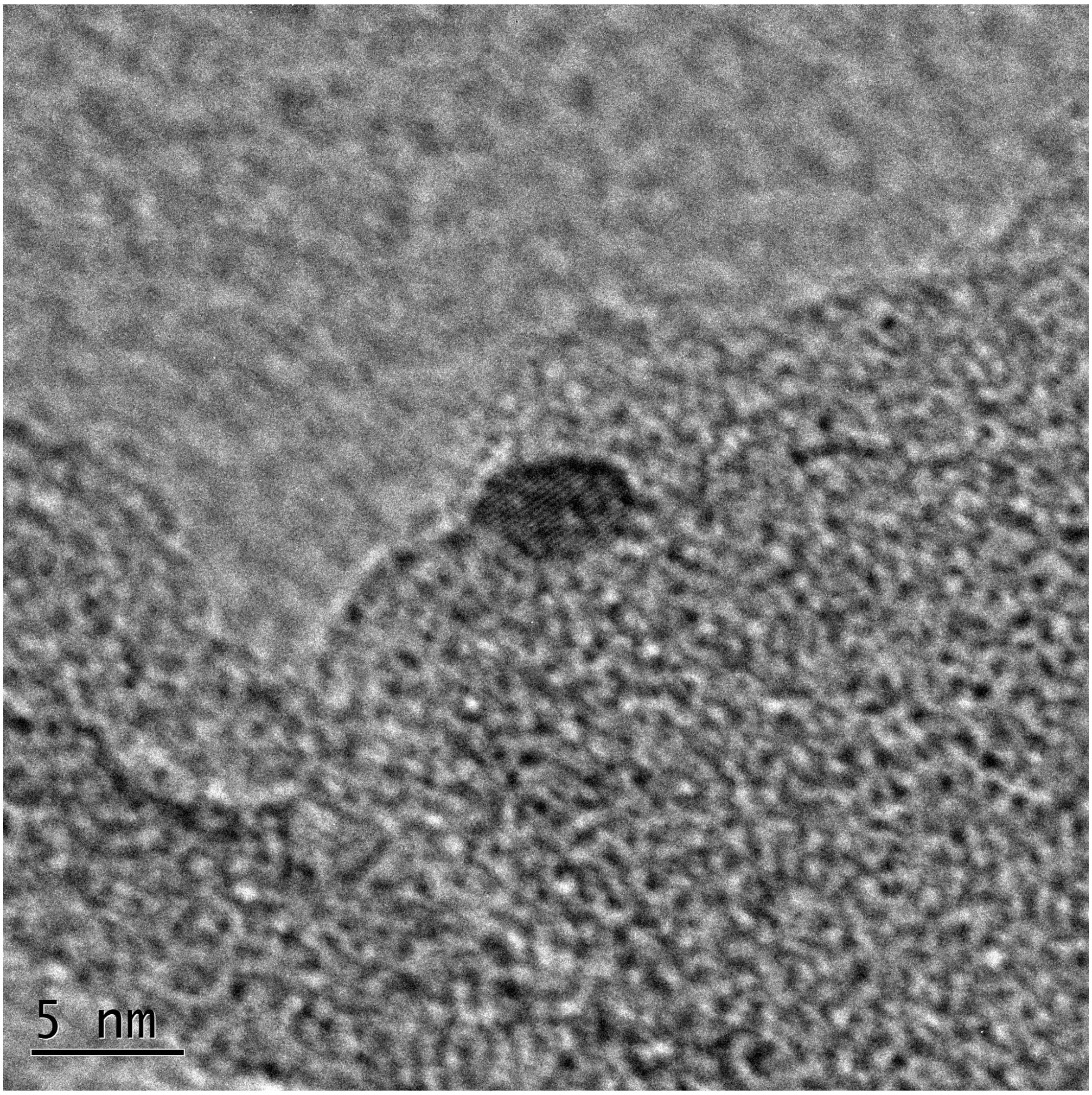

Figure 18. The TEM picture of the CNS/BOCB-OV after photo-deposition experiment

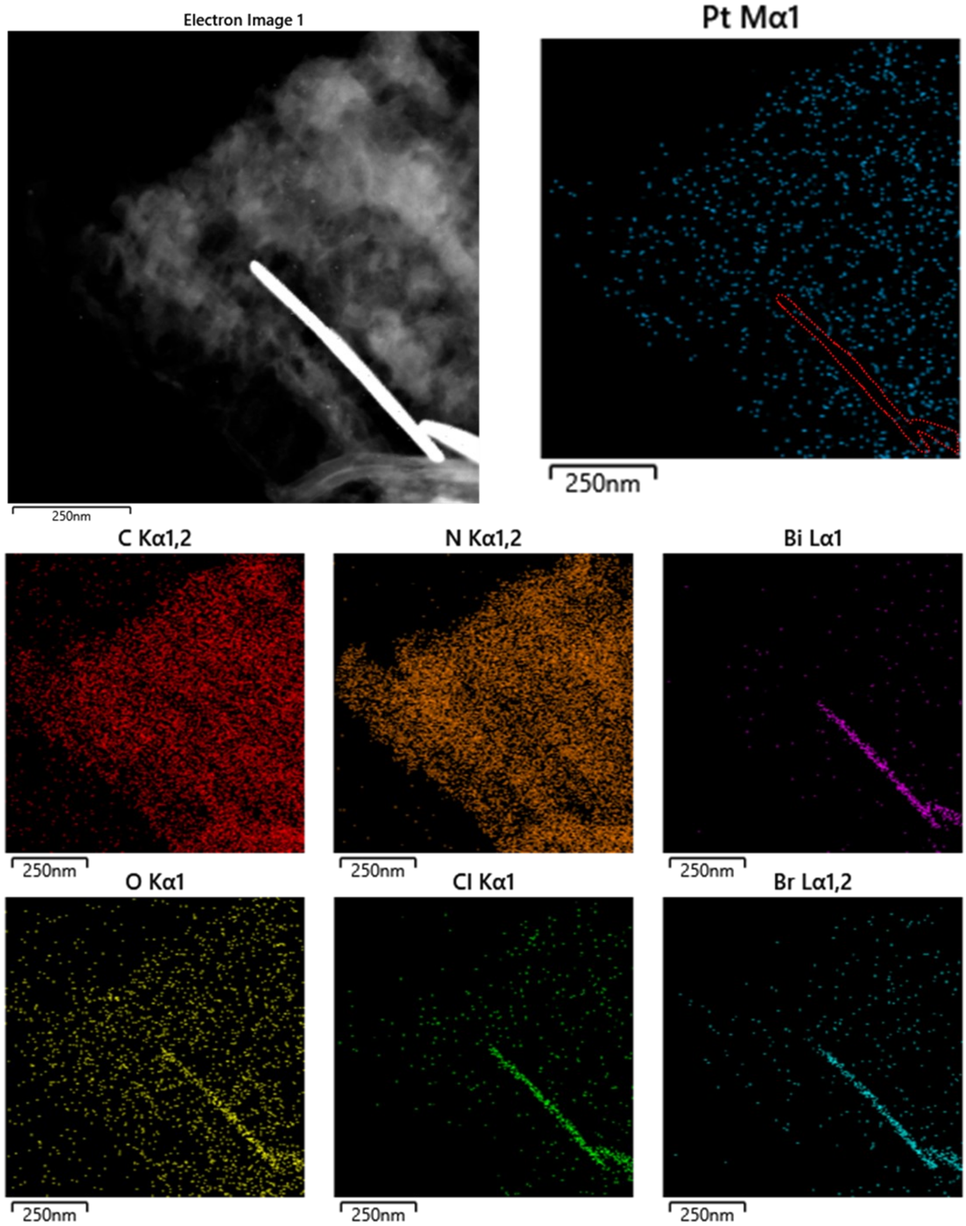

Figure 19. The TEM picture and the Pt, C, N, Bi, O, Cl, Br elemental mapping after photo-deposition experiment

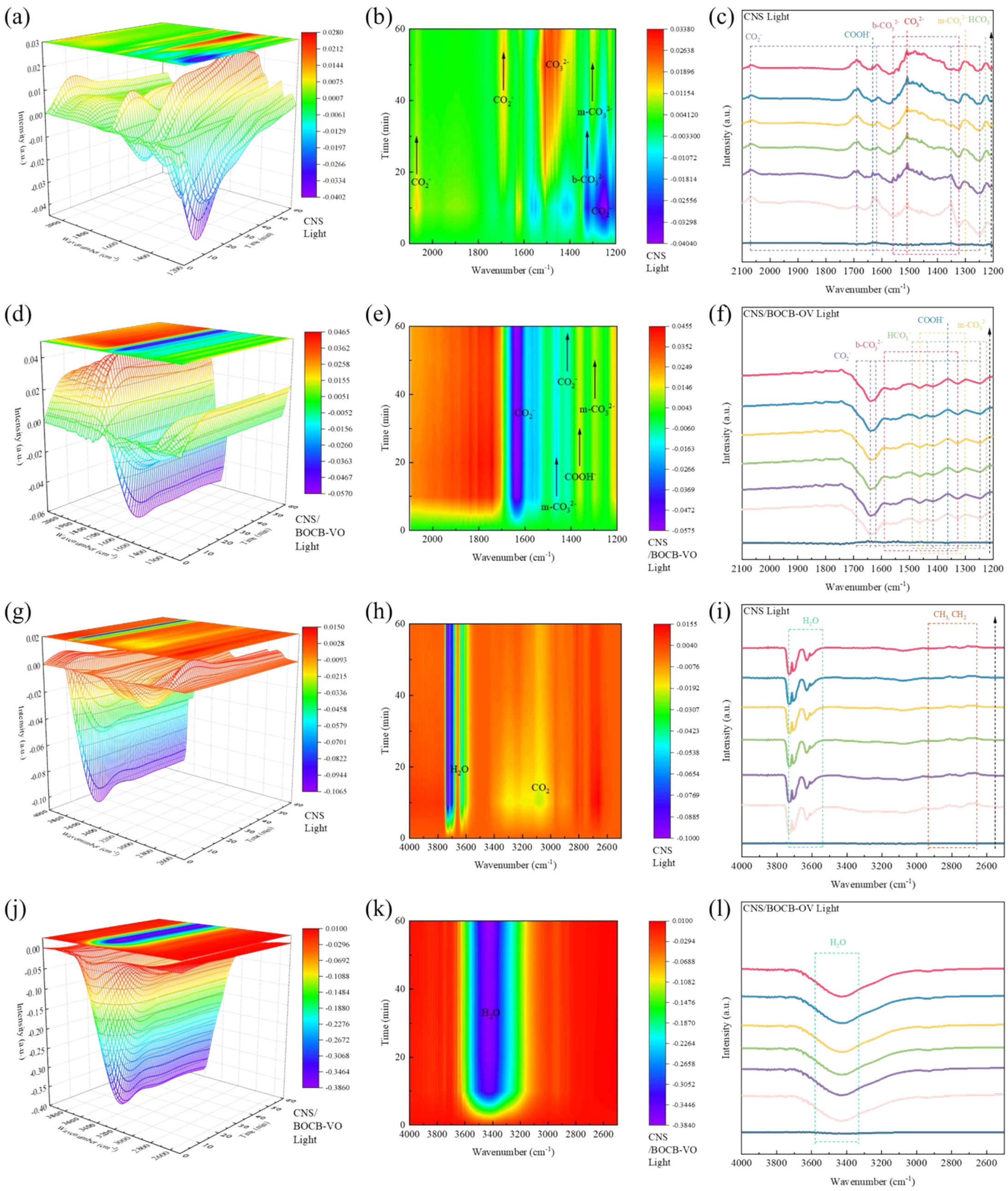

Fig. S20. In situ DRIFTS test of CO_2 and H_2O interaction with (a)-(c), (g)-(i) CNS and (d)-(f), (j)-(l) CNS/BOCB-OV under visible light irradiation

7. Supplementary Tables

Table S1. Atomic ratios of carbon and nitrogen species in CNS and CNS-HT.

Catalysts	Carbon species (at%)			Nitrogen species (at%)			O (at%)
	C-C	N=C-N	$C\text{-}NH_x$	C=N-C	$N\text{-}[C]_3$	$C\text{-}NH_x$	
CNS	9.41	31.99	3.57	32.99	6.94	12.86	2.24
CNS-HT	12.41	30.37	3.21	32.49	11.45	6.39	3.32

Table S2. Results of elemental analysis of CNS and CNS-HT.

Catalysts	C/wt%	N/wt%	O/wt%	C:N	O:C
CNS	34.91	60.21	3.84	0.676	0.082
CNS-HT	34.42	57.65	6.81	0.697	0.148

Table S3. Comparison of the reaction conditions and photocatalytic activity with other catalysts for CO_2 reduction to CO.

Catalysts	Light	CO_2 RR Condition	CO Yield /μmol·g^{-1}·h^{-1}	Reference
BiOCl Nanosheets	500W Xe Lamp UV+Vis	CO_2+H_2O (g)	1.01	1
$PbBiO_2Br$	300W Xe Lamp Vis	CO_2+H_2O (l)	0.42	2
Defect Oxygen Vacancies $PbBiO_2Br$ Nanosheets	300W Xe Lamp Vis	CO_2+H_2O (l)	2.23	2
Defective Bi_2MoO_6 Ultrathin Nanosheets	300W Xe Lamp UV+Vis	CO_2+H_2O (l)	3.62	3
BiOBr Ultrathin Nanosheets	300W Xe Lamp Vis	CO_2+H_2O (g)	2.67	4
$Bi_4O_5Br_2$ Nanosphere	300W Xe Lamp Vis	CO_2+H_2O (g)	2.73	4
Ag@BiOBr	300W Xe Lamp Vis	CO_2+H_2O (l)	1.36	5
BiOBr-Au-I	300W Xe Lamp Vis	CO_2+H_2O (g)	2.56	6
Au-CNS-ZIF-9	300W Xe Lamp UV+Vis	CO_2+H_2O (l)	0.5	7
Partial disorder structured BiOI atomic layers	300W Xe Lamp UV+Vis	CO_2+H_2O (l)	3.20	8
BOC	300W Xe Lamp Vis	CO_2+H_2O (g)	0.44	This Work

I doped BiOBr modified N vacancy g-C_3N_4	300W Xe Lamp UV+Vis	CO_2+H_2O+TC (l)	4.51	9
g-C_3N_4/ BiOCl with oxygen defects	300W Xe Lamp UV+Vis	CO_2+H_2O (g)	4.73	10
Crystalline Carbon Nitride Supported Copper Single Atoms	300W Xe Lamp UV+Vis	CO_2+H_2O (g)	3.09	11
Core-shell $LaPO_4$/g-C_3N_4 nanowires	300W Xe Lamp UV+Vis	CO_2+H_2O (g)	4.56	12
ZnPc/$BiVO_4$ nanocomposite	300W Xe Lamp Vis	CO_2+H_2O (g)	0.97	13
MnC-ZnO CTSHS	300W Xe Lamp UV+Vis	CO_2+H_2O (g)	0.21	14
CNS/BOCB-OV	300W Xe Lamp Vis	CO_2+H_2O (g)	5.90	This Work

Table S4. The adsorption energy of CNS, CNS/BOCB-OV and CNS/BOCB-OV-Between at different sites.

Adsorption Site	Adsorption Energy (CNS)/eV	Adsorption Energy (CNS/BOCB-OV)/eV	Adsorption Energy (CNS/BOCB-OV-Between)/eV
A1-Hx	0.182	-0.032	0.064
A1-Hx(45°)	-0.104	-0.065	0.29
A1-Hx(-45°)	**-0.116**	-0.101	-0.001
A1-Hy	-0.072	-0.052	0.039
A1-V	0.014	-0.086	-
A2-Hx	0.278	0.215	1.15
A2-Hx(45°)	0.238	0.054	-
A2-Hx(-45°)	0.278	-0.056	0.933
A2-Hy	0.199	0.123	1.071
A2-V	0.190	-0.095	-
A3-Hx	0.007	-0.143	0.874
A3-Hx(45°)	-0.035	0.456	0.243
A3-Hx(-45°)	-0.023	0.521	0.124
A3-Hy	0.043	-0.042	-
A3-V	-0.031	-0.086	-
A4-Hx	0.003	0.074	0.012
A4-Hx(45°)	-0.060	0.112	-0.014
A4-Hx(-45°)	-0.035	0.236	-
A4-Hy	0.043	-0.039	0.541
A4-V	-0.031	-0.071	-
C1-Hx	3.646	-0.035	0.12
C1-Hx(45°)	-0.072	-0.11	0.214
C1-Hx(-45°)	-0.057	0.131	0.335

C1-Hy	-0.053	0.005	0.215
C1-V	-0.047	0.012	-
C2-Hx	0.164	-0.014	-0.045
C2-Hx(45°)	-0.033	-0.088	0.964
C2-Hx(-45°)	-0.017	-0.096	-0.085
C2-Hy	3.914	0.425	-0.012
C2-V	-0.006	0.012	-
N1-Hx	0.255	0.069	0.164
N1-Hx(45°)	-0.015	0.055	0.118
N1-Hx(-45°)	-0.006	-0.073	0.742
N1-Hy	-0.044	-0.064	-0.053
N1-V	-0.039	-0.1	-
N2-Hx	-0.095	-0.014	-0.142
N2-Hx(45°)	-0.076	**-0.175**	-0.186
N2-Hx(-45°)	-0.078	-0.053	**-0.243**
N2-Hy	1.961	0.556	-0.042
N2-V	-0.004	0.021	-
N3-Hx	0.165	-0.045	0.001
N3-Hx(45°)	0.154	-0.069	0.124
N3-Hx(-45°)	0.155	0.018	0.265
N3-Hy	0.212	0.745	0.873
N3-V	-0.005	0.004	-

Table S5. Assigned surface species of the characteristic wavenumbers on CNS and CNS/BOCB-OV.

Wavenumber/cm^{-1}	Species	Reference
1225	HCO_3^-	15
1248	CO_2^-	16
1301	$m\text{-}CO_3^{2}$	17
1328	$b\text{-}CO_3^{2-}$	16,18
1356	CO_2^-	15
1365	$COOH^-$	19
1416	CO_2^-	17
1436	HCO_3^-	20
1463	$m\text{-}CO_3^{2}$	17
1490	HCO_3^-	17
1514	CO_3^{2-}	19
1560	$b\text{-}CO_3^{2-}$	21
1590	$b\text{-}CO_3^{2-}$	18
1620	CO_2^-	22
1630	$COOH^-$	23
1640	CO_2^-	24
1689	CO_2^-	17
1691	CO_2^-	19
2070	CO_2^-	24
3536-3730	H_2O	25

8. References

1 L. Zhang, W. Wang, D. Jiang, E. Gao and S. Sun, *Nano Res.*, 2015, **8**, 821–831.
2 B. Wang, S.-Z. Yang, H. Chen, Q. Gao, Y.-X. Weng, W. Zhu, G. Liu, Y. Zhang, Y. Ye, H. Zhu, H. Li and J. Xia, *Appl. Catal. B Environ.*, 2020, **277**, 119170.
3 J. Di, X. Zhao, C. Lian, M. Ji, J. Xia, J. Xiong, W. Zhou, X. Cao, Y. She, H. Liu, K. P. Loh, S. J. Pennycook, H. Li and Z. Liu, *Nano Energy*, 2019, **61**, 54–59.
4 L. Ye, X. Jin, C. Liu, C. Ding, H. Xie, K. H. Chu and P. K. Wong, *Appl. Catal. B Environ.*, 2016, **187**, 281–290.
5 G. Liu, L. Wang, B. Wang, X. Zhu, J. Yang, P. Liu, W. Zhu, Z. Chen and J. Xia, *Chin. Chem. Lett.*, 2023, **34**, 107962.
6 X. Fang, C.-Y. Wang, L. Zhou, Q. Zeng, H.-D. Zhou, Q. Wang and G. Zhu, *J. Environ. Chem. Eng.*, 2023, **11**, 109986.
7 H. Zhou, P. Li, J. Liu, Z. Chen, L. Liu, D. Dontsova, R. Yan, T. Fan, D. Zhang and J. Ye, *Nano Energy*, 2016, **25**, 128–135.
8 J. Xiong, X. Zhu, J. Xia and J. Di, *Appl. Surf. Sci.*, 2023, **627**, 157338.
9 X. Jia, C. Hu, H. Sun, J. Cao, H. Lin, X. Li and S. Chen, *Appl. Catal. B Environ.*, 2023, **324**, 122232.
10 Y. Chen, F. Wang, Y. Cao, F. Zhang, Y. Zou, Z. Huang, L. Ye and Y. Zhou, *ACS Appl. Energy Mater.*, 2020, **3**, 4610–4618.
11 Y. Li, B. Li, D. Zhang, L. Cheng and Q. Xiang, *ACS Nano*, 2020, **14**, 10552–10561.
12 M. Li, L. Zhang, X. Fan, M. Wu, M. Wang, R. Cheng, L. Zhang, H. Yao and J. Shi, *Appl. Catal. B Environ.*, 2017, **201**, 629–635.
13 D. N. Liu, D. Y. Chen, N. J. Li, Q. F. Xu, H. Li, J. H. He and J. M. Lu, *Angew. Chem.-Int. Ed.*, 2020, **59**, 4519–4524.
14 M. Sayed, F. Xu, P. Kuang, J. Low, S. Wang, L. Zhang and J. Yu, *Nat. Commun.*, 2021, **12**, 4936.
15 R. Tang, X. Dong, J. Sheng, S. Xi, L. Zhang and F. Dong, *Appl. Catal. B Environ.*, 2022, **316**, 121661.
16 J. Sheng, Y. He, J. Li, C. Yuan, H. Huang, S. Wang, Y. Sun, Z. Wang and F. Dong, *ACS Nano*, 2020, **14**, 13103–13114.
17 X. Shi, X. Dong, Y. He, P. Yan and F. Dong, *Sci. Bull.*, 2022, **67**, 1137–1144.
18 J. Sheng, Y. He, M. Huang, C. Yuan, S. Wang and F. Dong, *ACS Catal.*, 2022, **12**, 2915–2926.
19 X. Zhao, M. Huang, B. Deng, K. Li, F. Li and F. Dong, *Chem. Eng. J.*, 2022, **437**, 135114.
20 A. I. Paksoy, B. S. Caglayan and A. E. Aksoylu, *Int. J. Hydrog. Energy*, 2020, **45**, 12822–12834.
21 X. Yang, S. Wang, N. Yang, W. Zhou, P. Wang, K. Jiang, S. Li, H. Song, X. Ding, H. Chen and J. Ye, *Appl. Catal. B Environ.*, 2019, **259**, 118088.
22 L. Liu and Y. Li, *Aerosol Air Qual. Res.*, 2014, **14**, 453–469.
23 X. Shi, X. Dong, Y. He, P. Yan, S. Zhang and F. Dong, *ACS Catal.*, 2022, 3965–3973.
24 M. Wang, M. Shen, X. Jin, J. Tian, M. Li, Y. Zhou, L. Zhang, Y. Li and J. Shi, *ACS Catal.*, 2019, **9**, 4573–4581.
25 L. J. Liu, C. Y. Zhao and Y. Li, *J. Phys. Chem. C*, 2012, **116**, 7904–7912.